Biosensors and Bioelectronics 287 (2025) 117691

Contents lists available at ScienceDirect

Biosensors and Bioelectronics

journal homepage: www.elsevier.com/locate/bios

Demonstration and structural basis of a therapeutic DNA aptamer for SARS-CoV-2 spike protein detection

Yujun Liu [a,b,1], Kaidong Wang [c,d,f,1], Weiguang Wang [a,b], Saarang Kashyap [a,b], Jonathan Jih [a,b,e], Anthony Imani [a,b], Tzung Hsiai [c,d,f,*], Z. Hong Zhou [a,b,e,**]

[a] California NanoSystems Institute, University of California at Los Angeles, Los Angeles, 90095, California, USA
[b] Department of Microbiology, Immunology and Molecular Genetics, University of California at Los Angeles, Los Angeles, 90095, California, USA
[c] Division of Cardiology, Department of Medicine, David Geffen School of Medicine, University of California Los Angeles, Los Angeles, CA, 90095, USA
[d] Department of Medicine, Greater Los Angeles VA Healthcare System, Los Angeles, CA, 90073, USA
[e] Molecular Biology Institute, University of California, Los Angeles (UCLA), Los Angeles, CA, 90095, USA
[f] Department of Bioengineering, Henry Samueli School of Engineering and Applied Science, University of California Los Angeles, Los Angeles, CA, 90095, USA

ARTICLE INFO

Keywords:
Aptamer
CryoEM
SARS-CoV-2
Receptor binding domain
Detection
Specificity

ABSTRACT

At the onset of the COVID-19 pandemic, the absence of rapid and precise diagnostic tools hindered early detection and response. To address this challenge, we developed a renewable electrochemical impedance biosensor (aptasensor) using a therapeutic DNA aptamer immobilized on a nanostructured gold nanoparticle/carbon nanotube (AuNP/CNT) electrode to detect the SARS-CoV-2 spike (S) protein receptor-binding domain (RBD). The aptasensor achieved a limit of detection of 0.19 pg mL^{-1} and a dynamic range from 1 to 10^5 pg mL^{-1}. Following regeneration with a 60-s pH 2.0 rinse, the sensor retained over 90% of its original signal across five cycles and remained stable after two weeks of ambient storage. Dual-mode readouts, utilizing impedance spectroscopy and surface plasmon resonance (SPR), confirmed binding specificity and reproducibility. Cryogenic electron microscopy (cryoEM) resolved the aptamer–S protein complex in the open conformation, revealing a bridge-like interaction with conserved residues Y489, N487, F486, and S477. These contacts remained functional despite Omicron BA.2 mutations (S477N, N501Y) and aligned with previously reported mutational data. Specificity was further supported by negative controls and structural consistency with known hACE2 binding footprints. These results establish a robust, low-cost biosensor platform combining reuse, structural insight, and variant tolerance. The aptasensor's scalability and adaptability make it a strong candidate for future diagnostic applications targeting evolving viral threats.

1. Introduction

The SARS-CoV-2 virus, a single-stranded positive-sense RNA virus of the *Coronaviridae* family, encodes four structural proteins in its genome: spike (S), envelope (E), membrane (M), and nucleocapsid (N) (Hoffmann et al., 2020). Among these, the S protein is critical for viral entry. It forms a homotrimer, with each monomer consisting of two subunits: S1, which binds to receptors, and S2, which mediates membrane fusion (Cai et al., 2020; Wrapp et al., 2020a). The RBD in the S1 subunit specifically binds to the human angiotensin-converting enzyme 2 (hACE2) receptor and alternates between "open" and "closed" conformations (Shang et al., 2020). After binding hACE2 in the open conformation, the S2 subunit undergoes proteolytic activation, exposing a fusion peptide that facilitates membrane fusion between the virus and the host cell (Benton et al., 2020; Xia et al., 2020; Yan et al., 2020). These processes highlight the S protein as a key target for neutralizing antibodies and vaccines.

The COVID-19 pandemic emphasized the need for scalable, accurate detection methods. Current diagnostics include molecular (e.g., reverse-

* Corresponding author. Division of Cardiology, Department of Medicine, David Geffen School of Medicine, University of California Los Angeles, Los Angeles, CA, 90095, USA.
** Corresponding author. California NanoSystems Institute, University of California at Los Angeles, Los Angeles, 90095, California, USA.
E-mail addresses: thsiai@mednet.ucla.edu (T. Hsiai), Hong.Zhou@ucla.edu (Z.H. Zhou).
[1] YL and KW contributed equally as first authors.

https://doi.org/10.1016/j.bios.2025.117691
Received 11 March 2025; Received in revised form 23 May 2025; Accepted 11 June 2025
Available online 12 June 2025
0956-5663/© 2025 Elsevier B.V. All rights are reserved, including those for text and data mining, AI training, and similar technologies.

transcriptase polymerase chain reaction, RT-PCR), immunological (e.g., enzyme-linked immunosorbent assays, ELISA), and imaging techniques. While RT-PCR offers high sensitivity and specificity, it requires specialized infrastructure and is vulnerable to mutations in viral target sequences (Artika et al., 2022; Samson et al., 2020). Additionally, immunological assays are faster but demand technical expertise (Khan et al., 2022), while imaging is labor-intensive and costly (Shi et al., 2020). These limitations highlight the need for rapid, accessible, and mutation-resilient diagnostics.

Biosensors represent a promising alternative to traditional diagnostic methods. Such sensors convert biological signals into measurable electrical outputs through optical, electrochemical, piezoelectric, or thermal modalities (Justino et al., 2016; Perumal and Hashim, 2014). They provide high sensitivity and scalability for point-of-care use (Pohanka, 2018), but face challenges in durability, reuse, and integration (Patel et al., 2023). Addressing these gaps is crucial to unlocking their full diagnostic potential.

Aptamers, single-stranded nucleic acids selected through the systematic evolution of ligands by exponential enrichment (SELEX) process, have emerged as transformative tools for biosensors, offering antibody-like specificity at lower cost, with greater chemical stability and easier modification (Kumar Kulabhusan et al., 2020; Sefah et al., 2010). Advances in machine learning have enabled more rapid aptamer optimization for mutating viral targets (Bashir et al., 2021; Chen et al., 2021), making them ideal for flexible diagnostic platforms. In this study, we present the first cryoEM visualization of a SARS-CoV-2 aptamer complex designed for biosensor applications. The aptamer binds the RBD in the open conformation in two locations, forming a bridge-like interaction. This interaction informs rational re-engineering and highlights mutation-tolerant residue clusters suitable for long-term deployment.

To translate these insights into diagnostic utility, we developed a renewable electrochemical impedance biosensor ("aptasensor"), incorporating a thiol-functionalized anti-SARS-CoV-2 S protein aptamer immobilized on gold nanoparticle-modified carbon nanotube electrodes. The device enabled rapid, dose-dependent detection of the Omicron BA.2 S protein and remained functional after low-pH regeneration, confirming reusability. This scalable, mutation-tolerant platform offers a compelling solution for SARS-CoV-2 detection and broader pandemic preparedness.

2. Materials and methods

2.1. Reagents

Gold (III) chloride hydrate (~52% Au basis), potassium chloride hydrate, sulfuric acid (95.0–98.0%), potassium hexacyanoferrate (II) trihydrate (≥98.5%), potassium ferricyanide (III) (99%), HEPES solution, Tween 20, glycine (≥98.5%), ethanol (≥99.5%), sodium chloride (≥99.0%), phosphate buffer solution (PBS, 1.0 M, pH 7.4), and bovine serum albumin (BSA) were obtained from Sigma-Aldrich. All reagents were chosen for their high purity to ensure consistency and reproducibility in sensor fabrication. Multi-walled carbon nanotubes (XFM01, 5–15 nm in diameter, 10–30 μm in length) were sourced from XFNANO Technology Co. Ltd. The anti-SARS-CoV-2 S protein aptamer CoV2-6C3 (5′- CGC AGC ACC CAA GAA CAA GGA CTG CTT AGG ATT GCG ATA GGT TCG G - 3′) (Sun et al., 2021) was synthesized and purified by Integrated DNA Technologies (IDT). Recombinant SARS-CoV-2 S protein (lyophilized and liquid forms) was purchased from ACROBiosystems (SPN-C5227, Newark, DE, USA). Ultrapure water (18.2 MΩ cm) was prepared using a Millipore purification system.

2.2. Electrochemical impedance tests

Electrochemical measurements were conducted using a Gamry Interface 1010 E workstation (Gamry Instruments, Inc., USA). Electrochemical impedance spectroscopy (EIS) was performed over a frequency range from 100 kHz to 0.1 Hz to capture relevant charge transfer dynamics, using an electrolyte solution containing 0.1 M KCl, and 5 mM $[Fe(CN)_6]^{3-/4-}$. This composition was selected to facilitate electron transfer between the electrode and the analyte. The Randles model was used to fit the EIS data, with charge transfer resistance (R_{ct}) values extracted to evaluate aptamer binding events and sensor performance (Vivier and Orazem, 2022).

2.3. Preparation of a label-free electrochemical impedance aptasensor

2.3.1. Carbon nanotube (CNT) dispersion and electrode preparation

A 2 mg/mL suspension of multi-walled CNTs in a 50:50 (v/v) water-ethanol mixture was sonicated for 2h to ensure uniform dispersion and to prevent aggregation. A glassy carbon electrode (GCE, 3 mm diameter) was polished with a 50 nm aqueous alumina slurry on a polishing cloth to enhance surface roughness and cleaned via ultrasonication in ethanol and water. The cleaned GCE was dried under a nitrogen gas stream to avoid contamination.

2.3.2. CNT Deposition and gold nanoparticle (AuNP) coating

5 μL of the CNT suspension was drop-cast onto the GCE surface and dried at room temperature to form a CNT-modified GCE (CNTs/GCE). AuNPs were electrochemically deposited onto the CNTs/GCE by cycling the potential in a solution of gold (III) chloride hydrate in 0.5 M H_2SO_4. The resulting AuNPs/CNTs/GCE served as the substrate for aptamer immobilization, with AuNPs enhancing conductivity and providing a binding platform for thiolated aptamers.

2.3.3. Aptamer immobilization and blocking

A thiol-functionalized anti-SARS-CoV-2 S protein aptamer solution was incubated on the AuNPs/CNTs/GCE for 1h at room temperature to form a self-assembled monolayer. After aptamer immobilization, the electrode was rinsed with phosphate-buffered saline (PBS, pH 7.4) to remove unbound aptamers. To prevent non-specific binding, the surface of the electrode was treated with a 0.05% BSA solution in PBS for 30 min, followed by rinsing with PBS. The aptamer/AuNPs/CNTs/GCE electrochemical impedance aptasensor was stored at 4 °C for further use.

2.4. Surface plasmon resonance

Binding kinetics were analyzed using a Biacore 2000 system at 25 °C. The aptamer was immobilized onto a Series S Sensor Chip SA (GE Healthcare) in a running buffer containing 10 mM HEPES, 150 mM NaCl, pH 7.4, and 0.005 % (v/v) Tween-20. Serial dilutions of the SARS-CoV-2 S protein were injected at a flow rate of 30 μL/min, with association and dissociation phases lasting 180s and 900s, respectively. The chip surface was regenerated using a 0.1 M glycine-HCl buffer (pH 2) applied in two 10-s intervals. The optimized buffer composition ensured aptamer stability and reproducible sensor performance across cycles.

2.5. Negative-stain sample preparation and microscopy

Aptamer-conjugated AuNPs were incubated with SARS-CoV-2 S protein on ice for 30 min at a 1:1 M ratio. Glow-discharged Formvar-coated copper electron microscopy (EM) grids (Electron Microscopy Sciences, USA) were prepared by applying the sample for 1 min, blotting excess liquid, then washing three times with 2% uranyl acetate. A final incubation with uranyl acetate for 1 min provided contrast for imaging. Grids were dried at room temperature and imaged at 15,000c magnification using a Tecnai T12 microscope (Thermo Fisher Scientific, USA). Control samples were prepared using the same protocol without adding aptamers and used to verify specificity.

2.6. CryoEM sample preparation and imaging

The aptamer was incubated with thawed SARS-CoV-2 S protein (500 μg/dL) on ice for 30 min at a 4:1 M ratio of aptamer to S protein. A 4 μl aliquot of sample was applied to holey carbon Quantifoil R2/1 copper 200-mesh grids (Electron Microscopy Sciences, USA), blotted, and vitrified using a Vitrobot Mark IV (Thermo Fisher Scientific, USA) in a liquid ethane/propane mixture. Grids were screened in a Tecnai T20 (Thermo Fisher Scientific, USA) transmission electron microscope to optimize freezing conditions.

CryoEM data were collected on a 300 kV Titan Krios (Thermo Fisher Scientific, USA) equipped with a K3 direct electron detector (Gatan, USA) operated in electron counting mode. Movies were recorded at 81,000x magnification with a dose rate of 26.97 e^{-} $pixel^{-1}$ s^{-1}. 12,834 movies were captured, each comprising 40 frames with a total exposure time of 2 s. Automated image acquisition was accomplished using SerialEM (Mastronarde, 2018).

2.7. Data processing and 3D reconstruction

Data processing for 3D reconstruction was performed using CryoSPARC v4.3.1 and RELION-4.1 (Punjani et al., 2017; Scheres, 2012). Micrograph curation was performed to remove low-quality images before proceeding with particle picking. In total, 11,972 selected micrographs were subjected to patch motion correction using *MotionCor2* and CTF estimation using *GCTF* (Zhang, 2016; Zheng et al., 2017).

A previously published closed conformation map EMD-30660 (Xu et al., 2021) was used as a reference to generate templates for automated picking using *Template Picker* in CryoSPARC. These automatically picked particles were then subjected to iterative 2D classification, where the best classes were selected as templates for a second round of particle picking and subsequent 2D classification. The best classes were used to train a Topaz model (Bepler et al., 2019) for improved S protein particle picking. The trained Topaz model picked 1,175,879 particles, which were extracted at a box size of 330 Å (300 pixels) and filtered through additional rounds of 2D classification to remove junk particles, yielding a final dataset of 671,570 particles.

One round of homogeneous refinement on the extracted particles showed poorly resolved RBD densities in the resulting map, indicating that multiple S protein conformations were being averaged together. We performed 3D classification on the newly extracted particles and specified ten different classes to separate the S protein conformations. Subjecting these ten classes to heterogeneous refinement with the previous 3D classification volumes as references revealed two major classes corresponding to the open and closed conformation maps. Other classes generated from this heterogeneous refinement step were discarded due to poor alignment. The open and closed conformation 3D classes were then subjected to an additional round of heterogeneous refinement to remove contaminant or degraded particles. One round of non-uniform refinement (Punjani et al., 2020) in C1 symmetry was performed for both the open and the closed conformation map, followed by a C3 refinement for the closed conformation map due to the symmetrical positioning of the down RBDs. This helped improve the resolution of the closed conformation map to 3.4 Å (Table S1).

To better resolve the aptamer-RBD interaction in the open conformation map, additional data processing was carried out in RELION. A round of 3D classification was conducted on the entire structure to remove particles corresponding to closed and misaligned conformations, followed by a final round of global refinement. This refinement revealed a low-resolution helical density with distinct grooves binding to the open conformation up RBD. We confidently identified this density as the aptamer, as our aptamer model showed a strong structural match to this density and the density formed bridge-like contacts with the up RBD. To mitigate preferred orientation artifacts in the open conformation map, we performed anisotropic and misalignment correction using *spIsoNet* (Liu et al., 2025). Sharpening and postprocessing were performed on the half-maps generated from spIsoNet, yielding a final open confirmation map at 4.4 Å resolution (Table S1).

To assess structural variability of the up RBD in the open conformation, 3D variability analysis (Punjani and Fleet, 2021) was conducted in CryoSPARC, performed across three different modes with the "filter resolution (Å)" parameter set at 6 Å. A total of 20 volumes per mode was generated with volumes downsampled to 150px, capturing dynamic structural changes of the up RBD-aptamer complex. These volumes were compiled into a movie to visualize motion and flexibility (Movie S1), providing deeper insights into conformational dynamics and potential interactions.

2.8. Atomic model building and refinement

Initial model building was performed in Coot-0.8.9 (Emsley et al., 2010) and ISOLDE (Croll, 2018) using sharpened maps for both conformations: the open conformation model was adapted from PDB 7ND9 (Dejnirattisai et al., 2021), while the closed conformation model was derived from PDB 7DF3 (Xu et al., 2021). Models of the open conformation were flexibly fitted into our 3D variability maps to track positional changes of the up RBD. Model building of the aptamer structure was based on initial AlphaFold3 (Abramson et al., 2024) predictions of the CoV2-6C3 sequence, with further refinement to ensure correct base pairing of the aptamer. Following initial model building, amino acid residues of the S protein and nucleotides of the aptamer were both fixed via positional restraints. However, RBD residues involved in nucleotide recognition and interaction, as well as nucleotides predicted to interact with the RBD based on position and literature, were released from these constraints, along with their neighboring residues (Sun et al., 2021). Hypothesized RBD-aptamer interactions were simulated by implementing appropriate distance restraints for non-covalent forces between amino acids and nucleotides. Our ISOLDE simulation allowed us to flip out nucleotide bases and flexibly model non-covalent interactions with the aptamer residues conforming to our density map. Final refinements were performed in ISOLDE to optimize interactions between the aptamer and the up RBD. Structure visualization and figure preparation were done with UCSF ChimeraX (Meng et al., 2023).

3. Results

3.1. Development and performance of an electrochemical aptasensor for SARS-CoV-2 detection

The global urgency for rapid, sensitive, and scalable diagnostic tools has driven advancements in biosensor technology. Towards this end, we set out to develop an electrochemical impedance aptamer-based biosensor device, or aptasensor, leveraging a therapeutic aptamer sequence that targets the RBD of the SARS-CoV-2 S protein. To maximize the detection range of the aptasensor, CNTs were used as base electrodes due to their large specific surface area to better facilitate aptamer conjugation onto electrochemically deposited AuNPs (Fig. 1a). Electrochemical impedance spectroscopy (EIS) was used to monitor the charge-transfer resistance (R_{ct}) values, modeled using the Randles equivalent circuit model (Fig. 1b) (Vivier and Orazem, 2022). Nyquist plots revealed a semicircular region indicative of charge-transfer limitation at high frequencies, and a linear portion corresponding to diffusion-limitation at low frequencies (Vivier and Orazem, 2022). R_{ct} values increased proportionally with S protein concentrations, demonstrating specific adsorption and subsequent charge-transfer impedance in the presence of the $[Fe(CN)_6]^{3-/4-}$ redox probe. The aptasensor achieved a detection range of 1 pg mL^{-1} to 10^5 pg mL^{-1}, a strong linear correlation ($R^2 = 0.995$) (Fig. 1c), and a limit of detection (LOD) of 0.19 pg mL^{-1} (S/N = 3), outperforming prior SARS-CoV-2 biosensors (Wrobel, 2023; Zhu et al., 2020). This performance reflects the synergistic impact of CNT-enhanced sensitivity and aptamer specificity (Wongkaew et al., 2018). Notably, the biologically significant serum S

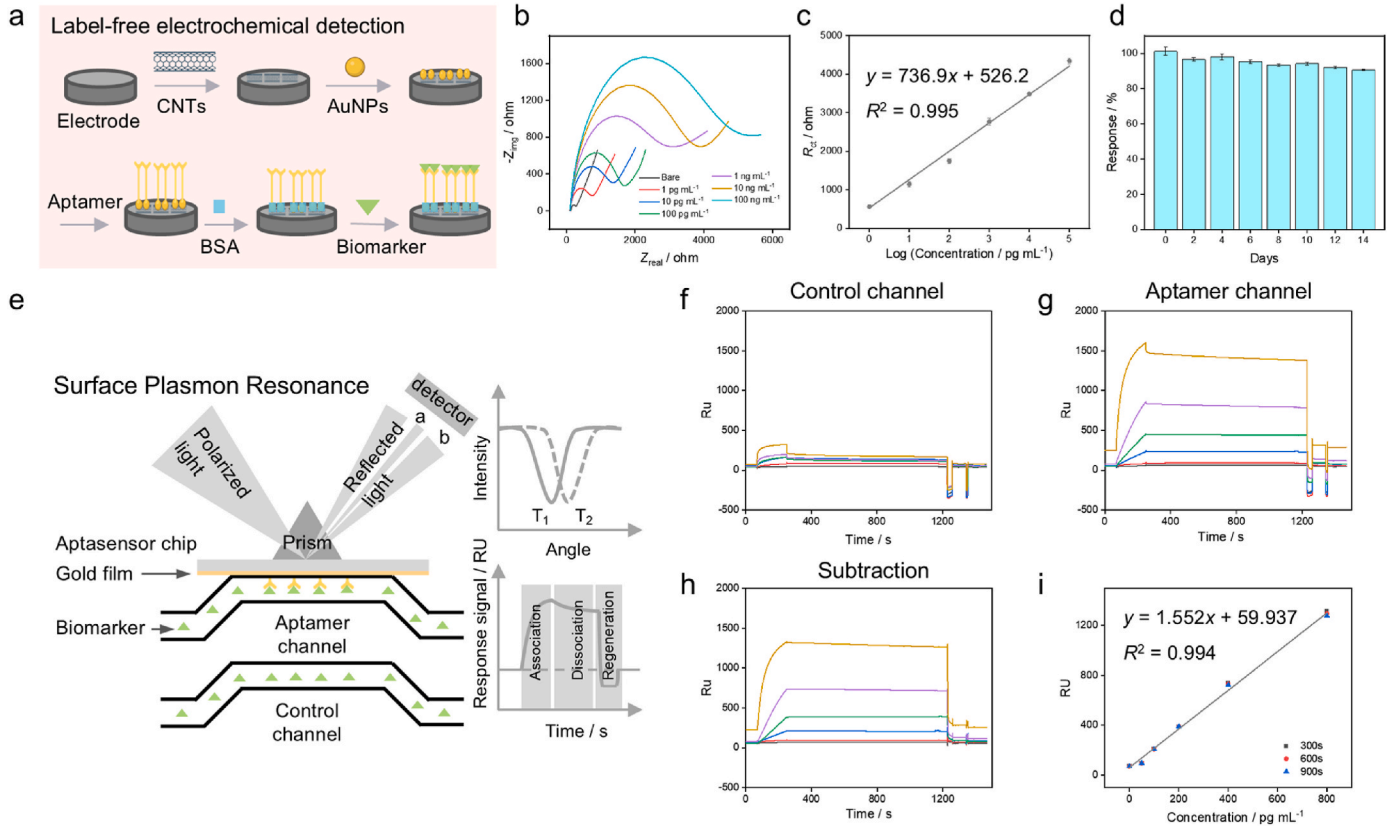

Fig. 1. Development and performance of aptasensor for SARS-CoV-2 S protein detection. (**a**) Schematic representation of the electrochemical impedance aptasensor fabrication process using CNTs, AuNPs, and an anti-SARS-CoV-2 S protein aptamer for selective detection. (**b**) EIS responses at different concentrations of SARS-CoV-2 S protein, ranging from 1 pg mL^{-1} to 10^5 pg/mL. (**c**) Calibration curve for correlating EIS response (R_{ct} values) with SARS-CoV-2 S protein concentrations, fitted using the Randles equivalent circuit model. (**d**) Long-term stability was established over 14 days. Error bars represent the SD from repeated measurements ($n = 3$). (**e**) Diagram illustrating the working principle of SPR detection for SARS-CoV-2 S protein detection using an aptamer-modified microfluidic chip. (**f**) SPR signal response recorded in the control channel without aptamer modification, indicating nonspecific adsorption. (**g**) SPR signal response observed in the aptamer functionalized channel, demonstrating specific binding to the SARS-CoV-2 S protein. (**h**) Subtracted SPR signal response to highlight the specific detection of the SARS-CoV-2 S protein by eliminating background signals from the control channels. (**i**) Calibration curve for SPR responses at different concentrations of SARS-CoV-2 S protein.

protein concentration, reported as 33.9 ± 22.4 pg mL^{-1} (Yonker et al., 2023), falls within the detection range of the aptasensor. Detection was achieved within 1h, highlighting its potential for real-time diagnostics. After two weeks of storage under ambient laboratory conditions, the sensor retained more than 90% of its initial signal response, demonstrating excellent long-term stability (Fig. 1d) when testing with PBS containing 100 pg mL^{-1} S protein. While direct imaging of all fabrication steps was not performed, consistent electrochemical baselines and aptamer attachment support proper sensor construction, as validated by immunogold TEM and cryoEM.

To assess the binding kinetics and specificity of the aptamer, we employed Surface Plasmon Resonance (SPR) (Fig. 1e). The SPR response increased proportionally with SARS-CoV-2 S protein concentrations, confirming high-affinity binding between the aptamer and the S protein (Fig. 1f–i) (Hanke et al., 2022). Regeneration studies using a 60-s rinse with 0.1 M glycine-HCl buffer (pH 2.0) demonstrated retention of over 90% of the original signal across five regeneration cycles, enabling cost-effective, multi-sample testing. This reversible binding is attributed to non-covalent forces, such as hydrogen bonding and van der Waals interactions (Williams et al., 2021). Structural resilience was further supported by aptamer recovery after pH exposure, consistent with prior reports of aptamer refolding under acidic conditions (Keefe et al., 2010). Three independently fabricated batches (n = 15) underwent repeated testing with 100 pg mL^{-1} S protein, with SPR results confirming consistent signal retention. The inter-sensor relative standard deviation (RSD) was 5.8%, and intra-sensor RSD was below 4.0%, confirming excellent reproducibility. The successful formation of CNT films and AuNP electrodeposition was indirectly validated by reproducible baseline electrochemical signatures, while aptamer attachment was confirmed via immunogold TEM and cryoEM. Collectively, these results demonstrate the aptasensor's high specificity, regeneration capacity, reproducibility, and potential for scalable diagnostic deployment. Comparative platform performance is summarized in Table S2, regeneration data across devices are detailed in Table S3, and individual R_{ct} values are detailed in Table S4.

3.2. CryoEM reveals aptamer-S protein interactions

We used immunogold labeling to confirm the presence of aptamer-conjugated AuNPs, visualizing their association with S protein via negative-stain EM (Fig. 2a). Initial cryoEM studies using lyophilized S protein revealed that it had lost its ability to interact with the aptamer. To determine the structure of the aptamer-S protein complex, we recorded ~12,000 movies using cryoEM with liquid S protein and subjected our extracted S protein particles to single particle analysis (Fig. 2b). Extensive 3D classification and heterogeneous refinement revealed two major classes with distinct differences in RBD positioning and aptamer interactions (Fig. 2c). We designated these two classes as the open and closed conformations, consistent with previous studies (Ye et al., 2022). Further 3D refinement led to an open confirmation map at a resolution of 4.4 Å and a closed conformation map at 3.4 Å.

The open conformation of the S protein consists of one RBD in an

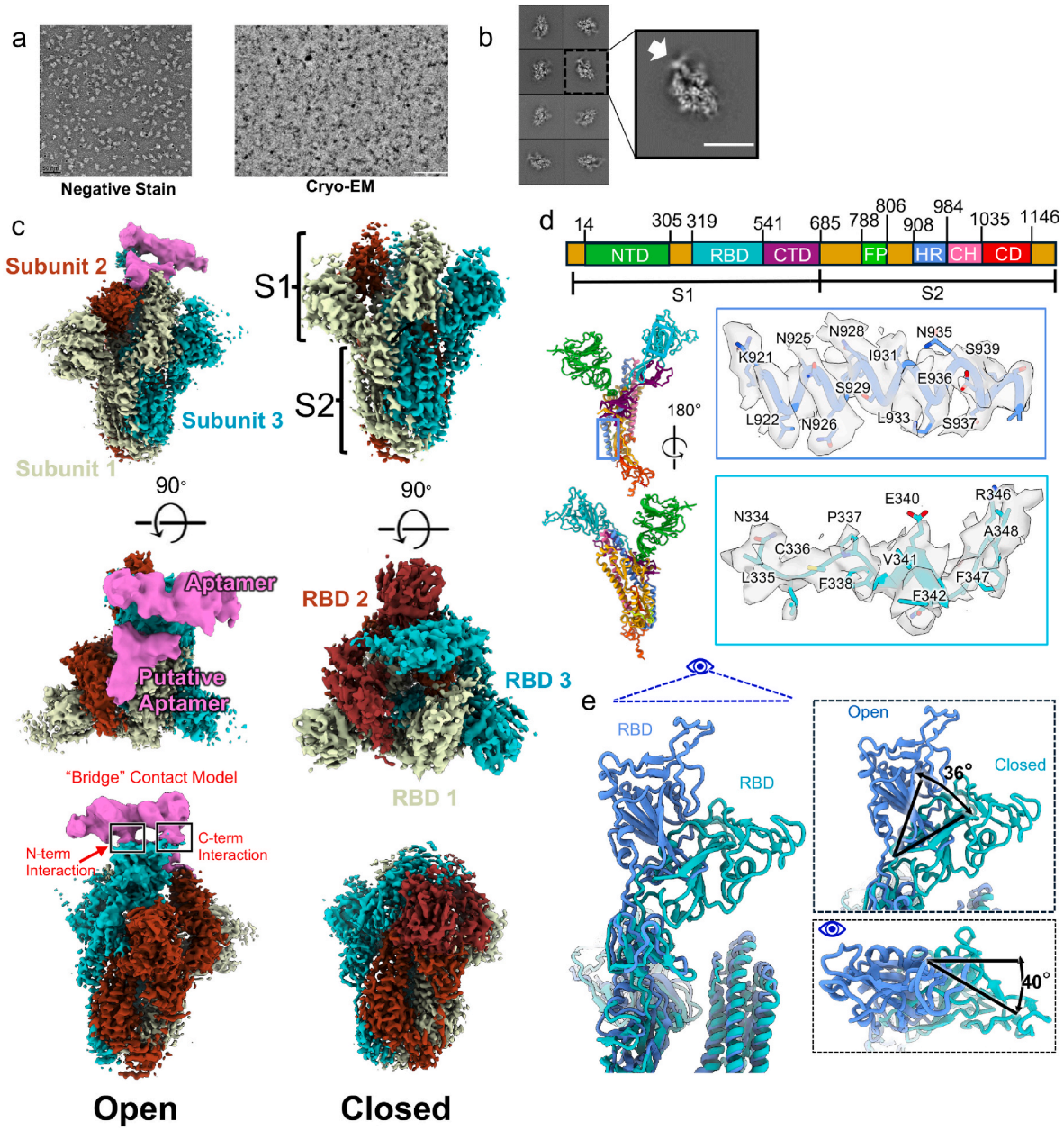

Fig. 2. Structural analysis of aptamer binding to SARS-CoV-2 S protein trimer. (**a**) Representative micrographs of negative-stain microscopy of aptamer-conjugated gold nanoparticles bound to S protein (Scale bar: 50 nm) and of cryoEM of aptamer-S protein complexes (Scale bar: 100 nm). (**b**) Representative 2D class averages of aptamer-S protein complexes in cryoEM images, with aptamer density interfacing with the receptor-binding domain (RBD) indicated by a white arrow. Scale bar: 135 Å (**c**) Maps of the S protein in open and closed conformations, with the aptamer densities in pink and N and C term bridge-contact between aptamer and RBD boxed and labeled (**d**) Labeled domains of full-length SARS-CoV-2 S protein. The S1 subunit contains NTD, RBD, and CTD, while S2 contains FP, HR1, CH, and CD. (**e**) Comparison of RBD positioning between open and closed conformations. (For interpretation of the references to colour in this figure legend, the reader is referred to the Web version of this article.)

upright position (up RBD) and two in the lying-down position (down RBD), with the aptamer bound to the up RBD. The nucleotide bases of the aptamer bind to the residues of the RBD at two distinct locations, forming a bridge-like interaction similar to the hACE2 interaction model (Wrapp et al., 2020b). Additionally, we observed a second sickle-shaped density that is positioned in the cleft formed by the two down RBDs and the one up RBD; we temporarily assign this as a putative aptamer density due to its positioning atop residues in the RBD which have been implicated in aptamer binding by previous molecular docking (MD) simulations (Sun et al., 2021). In contrast, the closed conformation has all three RBDs in the down position with no residues exposed for aptamer binding.

To gain further insight into RBD–aptamer interactions and positioning, we atomically modeled the open and closed S protein conformations, assigning domains to our monomers based on established literature: N-terminal Domain (14–305), RBD (319–541), C-terminal Domain (541–685), Fusion Peptide (788–806), Heptapeptide Repeat Sequence 1 (908–984), Central Helix (984–1035) and Connector Domain (1035–1146) (Yan et al., 2020) (Fig. 2d). Our modeling of the S1 (residues 1–685) and S2 (residues 686–1164) subunits revealed that while the S2 domains remain relatively rigid, the RBDs within S1 exhibit greater flexibility (Movie S1). In the S1 domain, the up RBD is elevated ~3.7 nm from the down RBD, with an approximate 36° angle between and a 40° angle out of the page rotation of the down RBD compared to

the up RBD (Fig. 2e). These findings highlight the position of the up RBD in aptamer recognition, providing a structural framework to understand aptamer-based detection strategies.

3.3. Positional variability and interactions of aptamer-RBD complex

The open conformation of the S protein binds the aptamer through its up RBD, forming a complex nearly perpendicular to adjacent monomer NTDs. To characterize the flexibility of this aptamer-RBD complex, we employed 3D Variability Analysis (3DVAR) in cryoSPARC to model its movement relative to the rest of the S protein (Fig. 3a). Our results revealed that the aptamer-RBD complex shifted up to 2 nm towards the adjacent down RBD, transitioning from a "straight" conformation to a "bent" conformation (Fig. 3b). Notably, the aptamer-RBD complex transiently shifts between the straight and bent conformations, showing strong binding to both conformations but reduced aptamer binding in the transition between them (Movie S1).

To further characterize the bridge-like interface between the aptamer and the RBD, we modeled putative interactions at the C-terminal region (residues 445–490) and the N-terminal region (residues 490–505) of the S protein RBD in the RBD-aptamer interface. Since our map precluded atomic modeling of interactions at the aptamer-RBD interface, we leveraged ISOLDE, a density-guided simulation software, to reveal potential binding mechanisms of the aptamer to the RBD. ISOLDE simulations steered the fitting of both S protein residues and aptamer nucleotides into the map, while considering non-covalent interactions (hydrogen bonds, ionic interactions, and van der Waals forces) and maintaining geometry constraints (bond lengths and angles) for protein and nucleic acid components. Based on our simulations, we propose that the aptamer interacts with the C-terminal cluster of RBD

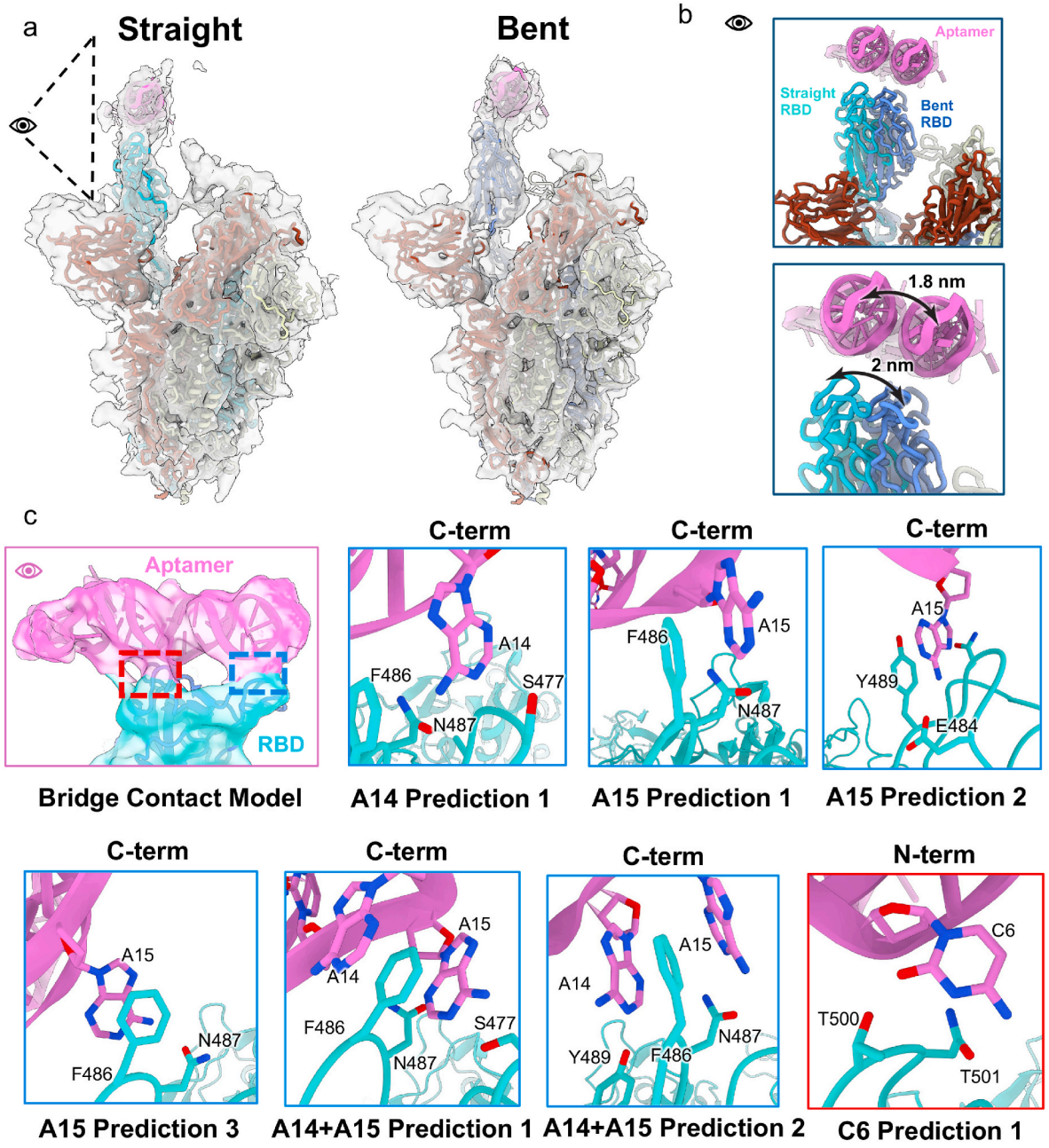

Fig. 3. Flexibility of aptamer-RBD complex and density-guided simulations of aptamer binding interactions. (**a**) 3D Flexibility of the open conformation in the Straight and Bent positions. (**b**) Shift in the aptamer-RBD position from straight to bent conformation. (**c**) Density-guided ISOLDE simulations of interactions between aptamer nucleotides and RBD residues at the C- and N-terminal regions of the RBD.

amino acids Y489, N487, F486, and S477 via unpaired nucleotides A14 and A15, consistent with previous aptamer mutagenesis studies (Sun et al., 2021) (Fig. 3c). At the N-terminal region, C6 likely interacts with N501, a residue previously implicated in hydrogen bonding with hACE2 residues (Yan et al., 2020). While the resolution in this region limits atomic modeling of nucleotide-residue interactions, we propose aptamer binding to occur through a combination of hydrogen bonding between polar or charged amino acids (e.g., N487 and S477) and unpaired nucleotides, along with π-stacking interactions between unpaired bases and aromatic residues (e.g., F486) (Fig. 3c). Overall, these forces likely strengthen binding affinity and maintain specificity of RBD-aptamer bridge contacts, even as the complex changes position.

4. Discussion

Our study establishes a renewable DNA-based aptasensor platform with high sensitivity and specificity for detecting the SARS-CoV-2 spike protein RBD, demonstrating the utility of aptamer-based technologies in pandemic response. Beyond validating the biosensor's detection capabilities, we used cryo-electron microscopy to visualize, for the first time, a therapeutic DNA aptamer bound to the open conformation of the SARS-CoV-2 S protein, offering mechanistic insight into aptamer-RBD interactions.

Importantly, the aptasensor platform demonstrated exceptional electrochemical performance. By integrating a nanostructured AuNP/CNT electrode with a thiol-functionalized DNA aptamer, we achieved a sub-picogram detection limit (0.19 pg mL^{-1}) and a broad dynamic range spanning five orders of magnitude, encompassing physiologically relevant viral loads.The LOD (~0.19 pg mL^{-1}) is well below serum S protein levels in COVID patients, indicating clinical potential. Unlike many conventional biosensors, our device supports regeneration through brief low-pH rinses while preserving aptamer integrity and function. Over 90% of the original signal was retained across five regeneration cycles, and the device remained stable after two weeks of room-temperature storage. The robustness of performance across independently fabricated devices and validation through dual-mode detection (impedance and SPR) positions this sensor as a practical tool for low-cost, point-of-care diagnostics.

In a broader context, our aptasensor addresses key limitations of existing diagnostic tools. Its regeneration capability significantly reduces per-test cost and waste, while its ultrasensitive detection range ensures utility in early-stage or asymptomatic cases. Unlike antibodies, aptamers can be rapidly synthesized, easily modified, and adapted to evolving targets. This modularity offers a powerful framework for future biosensor platforms targeting other viral antigens, cytokines, or emerging pathogens.

Our cryoEM analysis revealed that aptamer binding occurs exclusively on the up RBD, consistent with prior observations that only the open conformation exposes critical binding epitopes. The bridge-like configuration of aptamer engagement across our termed "C- and N-terminal regions" of the RBD suggests that the aptamer mimics elements of hACE2 binding. Specifically, we observed that residues such as F486, N487, Y489, S477, and N501, critical for hACE2 interaction, also mediate aptamer binding (Boon et al., 2021; Sun et al., 2021; Yan et al., 2020). This overlap suggests that aptamers may act similar to competitive inhibitors, a hypothesis supported by previous mutagenesis studies and our simulation-guided modeling.

We further showed that the aptamer-RBD complex is tolerant to RBD flexibility. 3D variability analysis revealed that the aptamer remains bound across a continuum of RBD conformations, from extended to bent states, mirroring the conformational landscape explored during hACE2 engagement. This flexibility likely enhances the robustness of aptamer binding under physiological conditions, where spike protein dynamics are pronounced. Interestingly, we identified a secondary low-resolution density in the open conformation map that may correspond to an auxiliary aptamer-binding site bridging the interface between one up and two down RBDs. This density is absent in the closed conformation, suggesting conformation-specific accessibility. Although the resolution does not permit atomic modeling, its spatial localization near known aptamer contact residues supports its functional relevance.

Taken together, these structural and electrochemical results reveal a dynamic sensing interface capable of withstanding mechanical fluctuations in the S protein and repeated chemical regeneration. The aptamer's stable binding to conserved RBD residues ensures functionality against variants such as Delta and Omicron BA.2, where critical contact points (e.g., F486, Y489) are retained. These findings not only support aptamer-based diagnostics as a scalable alternative to antibody assays but also suggest therapeutic potential for aptamers as viral entry inhibitors through hACE2 mimicry.

This work highlights the diagnostic promise of aptamer-based sensors. Other impedance platforms using Au nanorods have shown SARS-CoV-2 detection (Shahdeo et al., 2022), but lack our regeneration capability (Goode et al., 2015). Lateral flow assays, while rapid, suffer from poor reusability and lower specificity (Prakashan et al., 2023; Shahdeo et al., 2022). The minimal sample requirement of the aptasensor makes it particularly suitable for resource-limited settings, supporting rapid, minimally invasive diagnostics crucial for scalable outbreak responses, an approach recently validated through successful clinical deployment of aptamer-based biosensors in nasopharyngeal SARS-CoV-2 detection (Shrikrishna et al., 2024). Our aptasensor's low sample requirement, dose-dependent detection, and reusability offer advantages for outbreak response and routine clinical use. Future studies should explore aptamer adaptation for other biomarkers and assess therapeutic potential through hACE2 competition assays.

5. Conclusion

We have developed a DNA-based aptasensor for SARS-CoV-2 S protein detection, demonstrating high sensitivity, specificity, and reusability. The aptasensor achieves detection within 1 hour, operating within biologically relevant S protein concentrations, underscoring its potential for real-time diagnostics. Our structural analysis provides insights into aptamer-RBD interactions, revealing a bridge-like binding mechanism and the flexible nature of the aptamer-RBD complex. While further optimization and clinical validation are needed, the combination of sensitivity, specificity, and scalability establishes aptasensors as promising tools for next-generation diagnostics and pandemic preparedness.

CRediT authorship contribution statement

Yujun Liu: Writing – review & editing, Writing – original draft, Visualization, Investigation, Formal analysis, Data curation, Conceptualization. **Kaidong Wang:** Writing – review & editing, Writing – original draft, Visualization, Investigation, Formal analysis, Data curation, Conceptualization. **Weiguang Wang:** Writing – review & editing, Writing – original draft, Visualization, Formal analysis. **Saarang Kashyap:** Writing – review & editing, Writing – original draft, Visualization, Formal analysis. **Jonathan Jih:** Writing – review & editing, Formal analysis. **Anthony Imani:** Writing – review & editing, Writing – original draft, Visualization, Formal analysis. **Tzung Hsiai:** Writing – review & editing, Supervision, Resources, Methodology, Funding acquisition, Conceptualization. **Z. Hong Zhou:** Writing – review & editing, Writing – original draft, Supervision, Resources, Project administration, Methodology, Funding acquisition, Conceptualization.

Additional information

All data needed to evaluate the conclusions in the paper are present in the paper and/or the Supplementary Information. Additional data related to this paper may be requested from the authors. A cryoEM density map of the C1 open conformation is deposited under accession

number EMD-49943, and cryoEM density maps of the C1 and C3 closed conformations are deposited in EMDB under EMD-49927 and EMD-49928, respectively.

Funding

This work was supported by grants from the National Institutes of Health (NIH) to T.K.H. (R01HL149808, R01HL118650, R01HL159970, R01HL129727, and T32HL144449) and to Z.H.Z. (R01GM071940 and R01DE025567), and from VA I01BX004356 (T.K.H.).

Declaration of competing interest

The authors declare that they have no known competing financial interests or personal relationships that could have appeared to influence the work reported in this paper.

Acknowledgments

We acknowledge use of resources in the Electron Imaging Center for Nanomachines supported by UCLA and grants from the NIH (1S10OD018111) and the National Science Foundation (DBI-1338135 and DMR-1548924). Molecular graphics and analyses performed with UCSF ChimeraX, developed by the Resource for Biocomputing, Visualization, and Informatics at the University of California, San Francisco, with support from National Institutes of Health R01-GM129325 and the Office of Cyber Infrastructure and Computational Biology, National Institute of Allergy and Infectious Diseases.

Appendix A. Supplementary data

Supplementary data to this article can be found online at https://doi.org/10.1016/j.bios.2025.117691.

Data availability

Data will be made available on request.

References

Abramson, J., Adler, J., Dunger, J., Evans, R., Green, T., Pritzel, A., Ronneberger, O., Willmore, L., Ballard, A.J., Bambrick, J., Bodenstein, S.W., Evans, D.A., Hung, C.-C., O'Neill, M., Reiman, D., Tunyasuvunakool, K., Wu, Z., Žemgulytė, A., Arvaniti, E., Beattie, C., Bertolli, O., Bridgland, A., Cherepanov, A., Congreve, M., Cowen-Rivers, A.I., Cowie, A., Figurnov, M., Fuchs, F.B., Gladman, H., Jain, R., Khan, Y.A., Low, C.M.R., Perlin, K., Potapenko, A., Savy, P., Singh, S., Stecula, A., Thillaisundaram, A., Tong, C., Yakneen, S., Zhong, E.D., Zielinski, M., Žídek, A., Bapst, V., Kohli, P., Jaderberg, M., Hassabis, D., Jumper, J.M., 2024. Accurate structure prediction of biomolecular interactions with AlphaFold 3. Nature 630 (8016), 493–500.
Artika, I.M., Dewi, Y.P., Nainggolan, I.M., Siregar, J.E., Antonjaya, U., 2022. Genes 13 (12).
Bashir, A., Yang, Q., Wang, J., Hoyer, S., Chou, W., McLean, C., Davis, G., Gong, Q., Armstrong, Z., Jang, J., Kang, H., Pawlosky, A., Scott, A., Dahl, G.E., Berndl, M., Dimon, M., Ferguson, B.S., 2021. Nat. Commun. 12 (1), 2366.
Benton, D.J., Wrobel, A.G., Xu, P., Roustan, C., Martin, S.R., Rosenthal, P.B., Skehel, J.J., Gamblin, S.J., 2020. Nature 588 (7837), 327–330.
Bepler, T., Morin, A., Rapp, M., Brasch, J., Shapiro, L., Noble, A.J., Berger, B., 2019. Nat. Methods 16 (11), 1153–1160.
Boon, S.S., Xia, C., Wang, M.H., Yip, K.L., Luk, H.Y., Li, S., Ng, R.W.Y., Lai, C.K.C., Chan, P.K.S., Chen, Z., 2021. mBio 12 (5). https://doi.org/10.1128/mbio.02687-02621.
Cai, Y., Zhang, J., Xiao, T., Peng, H., Sterling, S.M., Walsh, R.M., Rawson, S., Rits-Volloch, S., Chen, B., 2020. Science 369 (6511), 1586–1592.
Chen, Z., Hu, L., Zhang, B.T., Lu, A., Wang, Y., Yu, Y., Zhang, G., 2021. Int. J. Mol. Sci. 22 (7).
Croll, T., 2018. Acta Crystallogr. D 74 (6), 519–530.
Dejnirattisai, W., Zhou, D., Ginn, H.M., Duyvesteyn, H.M.E., Supasa, P., Case, J.B., Zhao, Y., Walter, T.S., Mentzer, A.J., Liu, C., Wang, B., Paesen, G.C., Slon-Campos, J., López-Camacho, C., Kafai, N.M., Bailey, A.L., Chen, R.E., Ying, B., Thompson, C., Bolton, J., Fyfe, A., Gupta, S., Tan, T.K., Gilbert-Jaramillo, J., James, W., Knight, M., Carroll, M.W., Skelly, D., Dold, C., Peng, Y., Levin, R., Dong, T., Pollard, A.J., Knight, J.C., Klenerman, P., Temperton, N., Hall, D.R., Williams, M.A., Paterson, N. G., Bertram, F.K.R., Siebert, C.A., Clare, D.K., Howe, A., Radecke, J., Song, Y., Townsend, A.R., Huang, K.-Y.A., Fry, E.E., Mongkolsapaya, J., Diamond, M.S., Ren, J., Stuart, D.I., Screaton, G.R., 2021. Cell 184 (8), 2183–2200.e2122.
Emsley, P., Lohkamp, B., Scott, W.G., Cowtan, K., 2010. Acta Crystallogr D Biol Crystallogr 66 (Pt 4), 486–501.
Goode, J.A., Rushworth, J.V.H., Millner, P.A., 2015. Langmuir 31 (23), 6267–6276.
Hanke, L., Das, H., Sheward, D.J., Perez Vidakovics, L., Urgard, E., Moliner-Morro, A., Kim, C., Karl, V., Pankow, A., Smith, N.L., 2022. Nat. Commun. 13 (1), 155.
Hoffmann, M., Kleine-Weber, H., Pöhlmann, S., 2020. Mol. Cell 78 (4), 779–784.e775.
Justino, C.I.L., Duarte, A.C., Rocha-Santos, T.A.P., 2016. TrAC, Trends Anal. Chem. 85, 36–60.
Keefe, A.D., Pai, S., Ellington, A., 2010. Nat. Rev. Drug Discov. 9 (7), 537–550.
Khan, S.H., Zaidi, S.K., Gilani, M., 2022. J. Pakistan Med. Assoc. 72 (6), 1166–1174.
Kumar Kulabhusan, P., Hussain, B., Yüce, M., 2020. Pharmaceutics 12 (7).
Liu, Y.T., Fan, H., Hu, J.J., Zhou, Z.H., 2025. Nat. Methods 22 (1), 113–123.
Mastronarde, D.N., 2018. Microsc. Microanal. 24 (S1), 864–865.
Meng, E.C., Goddard, T.D., Pettersen, E.F., Couch, G.S., Pearson, Z.J., Morris, J.H., Ferrin, T.E., 2023. Protein Sci. 32 (11), e4792.
Patel, S.K., Surve, J., Parmar, J., Ahmed, K., Bui, F.M., Al-Zahrani, F.A., 2023. IEEE Rev Biomed Eng 16, 22–37.
Perumal, V., Hashim, U., 2014. J. Appl. Biomed. 12 (1), 1–15.
Pohanka, M., 2018. Materials 11 (3).
Prakashan, D., Shrikrishna, N.S., Byakodi, M., Nagamani, K., Gandhi, S., 2023. J. Med. Virol. 95 (1), e28416.
Punjani, A., Fleet, D.J., 2021. J. Struct. Biol. 213 (2), 107702.
Punjani, A., Rubinstein, J.L., Fleet, D.J., Brubaker, M.A., 2017. Nat. Methods 14 (3), 290–296.
Punjani, A., Zhang, H., Fleet, D.J., 2020. Nat. Methods 17 (12), 1214–1221.
Samson, R., Navale, G.R., Dharne, M.S., 2020. 3 Biotech 10 (9), 385.
Scheres, S.H.W., 2012. J. Struct. Biol. 180 (3), 519–530.
Sefah, K., Shangguan, D., Xiong, X., O'Donoghue, M.B., Tan, W., 2010. Nat. Protoc. 5 (6), 1169–1185.
Shahdeo, D., Roberts, A., Archana, G.J., Shrikrishna, N.S., Mahari, S., Nagamani, K., Gandhi, S., 2022. Biosens. Bioelectron. 212, 114406.
Shang, J., Wan, Y., Luo, C., Ye, G., Geng, Q., Auerbach, A., Li, F., 2020. Proceedings of the. National Academy of Sciences 117 (21), 11727–11734.
Shi, R., Shan, C., Duan, X., Chen, Z., Liu, P., Song, J., Song, T., Bi, X., Han, C., Wu, L., Gao, G., Hu, X., Zhang, Y., Tong, Z., Huang, W., Liu, W.J., Wu, G., Zhang, B., Wang, L., Qi, J., Feng, H., Wang, F.-S., Wang, Q., Gao, G.F., Yuan, Z., Yan, J., 2020. Nature 584 (7819), 120–124.
Shrikrishna, N.S., Halder, S., Kesarwani, V., Nagamani, K., Gandhi, S., 2024. Chem. Eng. J. 493, 152841.
Sun, M., Liu, S., Wei, X., Wan, S., Huang, M., Song, T., Lu, Y., Weng, X., Lin, Z., Chen, H., Song, Y., Yang, C., 2021. Angew Chem. Int. Ed. Engl. 60 (18), 10266–10272.
Vivier, V., Orazem, M.E., 2022. Chem. Rev. 122 (12), 11131–11168.
Williams, G.T., Haynes, C.J., Fares, M., Caltagirone, C., Hiscock, J.R., Gale, P.A., 2021. Chem. Soc. Rev. 50 (4), 2737–2763.
Wongkaew, N., Simsek, M., Griesche, C., Baeumner, A.J., 2018. Chem. Rev. 119 (1), 120–194.
Wrapp, D., Wang, N., Corbett, K.S., Goldsmith, J.A., Hsieh, C.-L., Abiona, O., Graham, B. S., McLellan, J.S., 2020a. Science 367 (6483), 1260–1263.
Wrapp, D., Wang, N., Corbett, K.S., Goldsmith, J.A., Hsieh, C.-L., Abiona, O., Graham, B. S., McLellan, J.S., 2020b. Science 367 (6483), 1260–1263.
Wrobel, A.G., 2023. Curr. Opin. Struct. Biol. 81, 102619.
Xia, S., Liu, M., Wang, C., Xu, W., Lan, Q., Feng, S., Qi, F., Bao, L., Du, L., Liu, S., Qin, C., Sun, F., Shi, Z., Zhu, Y., Jiang, S., Lu, L., 2020. Cell Res. 30 (4), 343–355.
Xu, C., Wang, Y., Liu, C., Zhang, C., Han, W., Hong, X., Wang, Y., Hong, Q., Wang, S., Zhao, Q., Wang, Y., Yang, Y., Chen, K., Zheng, W., Kong, L., Wang, F., Zuo, Q., Huang, Z., Cong, Y., 2021. Conformational dynamics of SARS-CoV-2 trimeric spike glycoprotein in complex with receptor ACE2 revealed by cryo-EM. Sci. Adv. 7 (1), eabe5575.
Yan, R., Zhang, Y., Li, Y., Xia, L., Guo, Y., Zhou, Q., 2020. Science 367 (6485), 1444–1448.
Ye, G., Liu, B., Li, F., 2022. Nat. Commun. 13 (1), 1214.
Yonker, L.M., Swank, Z., Bartsch, Y.C., Burns, M.D., Kane, A., Boribong, B.P., Davis, J.P., Loiselle, M., Novak, T., Senussi, Y., Cheng, C.A., Burgess, E., Edlow, A.G., Chou, J., Dionne, A., Balaguru, D., Lahoud-Rahme, M., Arditi, M., Julg, B., Randolph, A.G., Alter, G., Fasano, A., Walt, D.R., 2023. Circulation 147 (11), 867–876.
Zhang, K., 2016. J. Struct. Biol. 193 (1), 1–12.
Zheng, S.Q., Palovcak, E., Armache, J.P., Verba, K.A., Cheng, Y., Agard, D.A., 2017. Nat. Methods 14 (4), 331–332.
Zhu, N., Zhang, D., Wang, W., Li, X., Yang, B., Song, J., Zhao, X., Huang, B., Shi, W., Lu, R., Niu, P., Zhan, F., Ma, X., Wang, D., Xu, W., Wu, G., Gao, G.F., Tan, W., 2020. N. Engl. J. Med. 382 (8), 727–733.